Experimental Study of Crack Closure on Heterogeneous Quasi-Brittle Material

Olivier Nouailletas, Christian La Borderie, Céline Perlot-Bascoules, Patrice Rivard, Gérard Balivy

Experimental Study of Crack Closure on Heterogeneous Quasi-Brittle Material

Olivier Nouailletas[1]; Christian La Borderie[2]; Céline Perlot[3]; Patrice Rivard[4]; and Gérard Ballivy[5]

Abstract: In civil engineering, the behavior of a cracked concrete is a major challenge with regard to the management of a structure's durability. The purpose of this experimental work is to better understand the behavior of a quasi-brittle cracked material at macro-scale, and to provide new data for numerical models. Cyclic compression/tension tests were performed on a notched concrete specimen. The effects of cracks' closure opening were investigated by classical measurements (displacement sensors) and digital image correlation. Damage and inelastic strains were exhibited when cracks propagate during the tensile phase. When the load is reversed to induce compressive stress, the effect of damage on the concrete stiffness was progressively reduced. A relation between the inelastic strains and the damage variable emerges, and it is proved that these two variables are not thermodynamically independent. The study on the crack lips' displacement shows that at least a part of the inelastic strain is due to the friction between the crack lips. The evolution of the damage and the dissipated energy during a loading cycle were also calculated, and results showed that the dissipated energy grows hyperbolically with the crack propagation.

Keywords: Cracking; Concrete; Cyclic test; Tension/compression; Inelastic strains; Friction.

Introduction

The computations of reinforced concrete elements under seismic loadings use damage and/or plasticity models that represented the behavior of concrete elements under cyclic loading. One of the major challenges faced during the development of these models is the simulation of microcrack closure reopening (MCR) (Wu and Xu 2013) involving the deactivation of the damage that can drive spurious dissipation (Berthaud et al. 1990; Carol and Willam 1996). The most refereed experimental studies on the uniaxial cyclic behavior of concrete are from Reinhardt and Cornelissen (1984), Reinhardt et al. (1986), Mazars and Berthaud (1989), and from Mazars et al. (1990). In the first refereed studies, the authors applied direct tension tests on a double-notched specimen, whereas in the second studies, the authors applied the load through aluminum bars glued to the concrete specimen to avoid strain localization. These studies are presented in Fig. 1. From these results, the behavior of the concrete exhibits damage and inelastic strains, and the stiffness is recovered in compressive mode; however, the evolution

of the inelastic strains when the load compressed is quite different. In Fig. 1(a), the inelastic strain decreases when the stress becomes negative and tends to be a zero constant, whereas in Fig. 1(b), the inelastic strains appear to tend asymptotically to be zero.

The way the inelastic strains behave in compression governs part of the structural behavior, especially around the zero-load zones. For instance, Fig. 2(a) shows the load deflection curve computed with a multifiber approach for a reinforced concrete beam subjected to a cyclic three-point loading (La Borderie et al. 1994). The span of the beam is 1.5 m, and the cross section is 0.2 m in height by 0.15 m in depth. The beam is reinforced with two 12-mm diameter bars in the upper and lower parts of the section. The experimental results and the numerical results from computations with an unilateral damage model with a closure function originally developed by La Borderie et al. (1994) are compared with those obtained by *pure damage* and pseudoplastic plastic models. For the pure damage model, the inelastic strains were null. For the model with a crack-closure function, the inelastic strains have been created together with damage progressively decreased when loaded in compression until the crack-closure stress (which is set here to 3 MPa) is reached. For the pseudoplastic set, the inelastic strains continue during compression loading. The results obtained for a uniaxial tension test are shown in Fig. 3.

The results obtained for the three-point bending must be compared with the experimental data shown in Fig. 2(b). It is obvious that the results computed with the *pseudoplasticity* set of parameters does not fit the experimental data and must be excluded. The study of the stabilized cycle reveals the classically unversed S shape found on structures subjected to cyclic loading. This result is obtained only with the crack-closure function set of parameters. This particular behavior exhibits a lower tangential stiffness around the zero load because of the way MCR are modeled and must be reproduced when computing structures are subjected to cyclic loading.

This paper presents experimental results obtained from direct-tension tests with cyclic loadings on concrete specimens: The effects of crack reclosing on quasi-brittle materials' behavior are studied at the macroscale. These experimental results could provide new data for modeling quasi-brittle material behavior.

---

[1]SIAME, EA 4581, Univ. of Pau, France; presently, SIAME Laboratory, 1 allée du parc Montaury, 64600 Anglet, France (corresponding author). E-mail: olivier.nouailletas@univ-pau.fr

[2]SIAME, EA 4581, Univ. of Pau, France; presently, SIAME Laboratory, 1 allée du parc Montaury, 64600 Anglet, France. E-mail: christian .laborderie@univ-pau.fr

[3]SIAME, EA 4581, Univ. of Pau, France; presently, SIAME Laboratory, 1 allée du parc Montaury, 64600 Anglet, France. E-mail: celine.perlot@ univ-pau.fr

[4]Département de Génie Civil, Université de Sherbrooke, 2500 boul. de l'UniversitØ, Sherbrooke, QC, Canada J1 K 2R1. E-mail: Patrice.Rivard@ USherbrooke.ca

[5]Département de Génie Civil, Université de Sherbrooke, 2500 boul. de l'Université, Sherbrooke, QC, Canada J1 K 2R1. E-mail: Ballivy.Gerard@ USherbrooke.ca
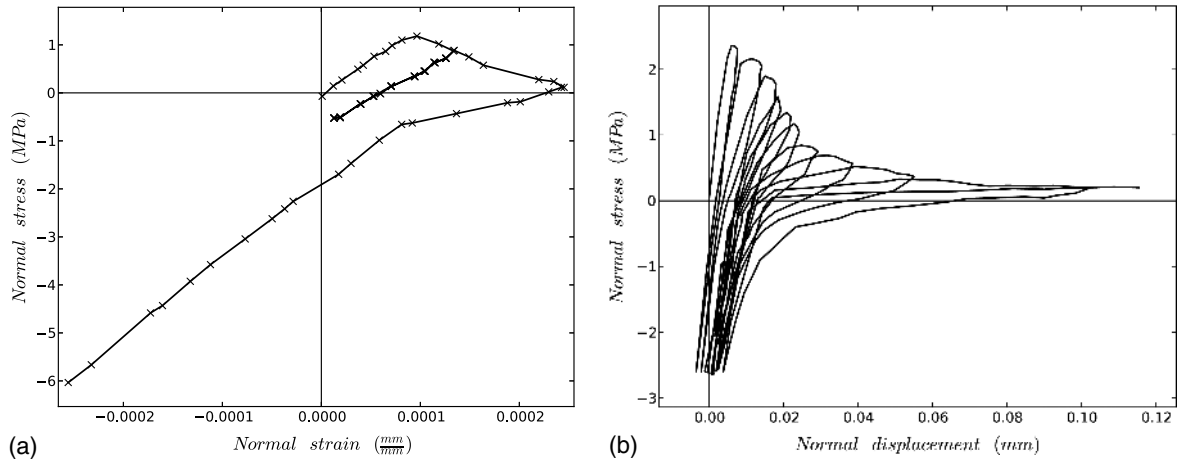
Fig. 1. Experimental behavior of concrete under cyclic tension: (a) Mazars and Berthaud data; (b) cornelissen data
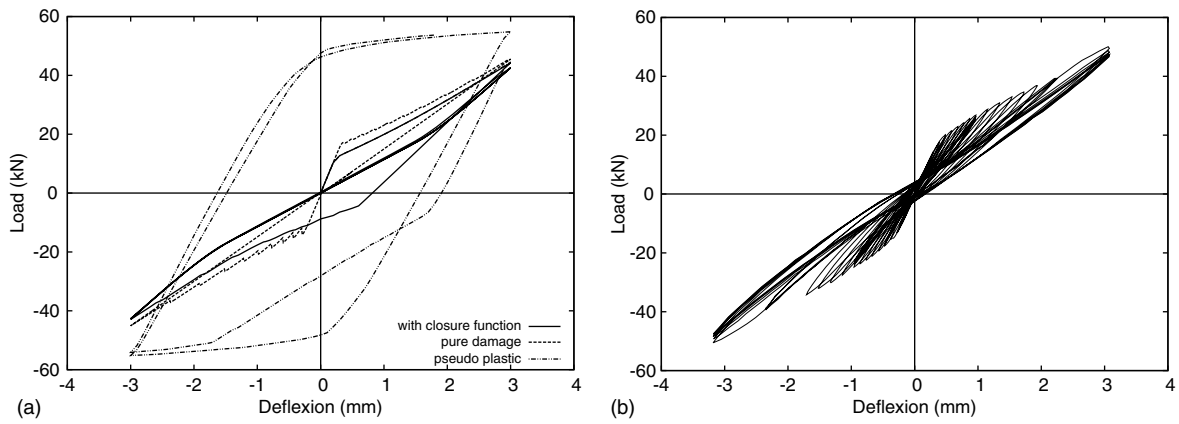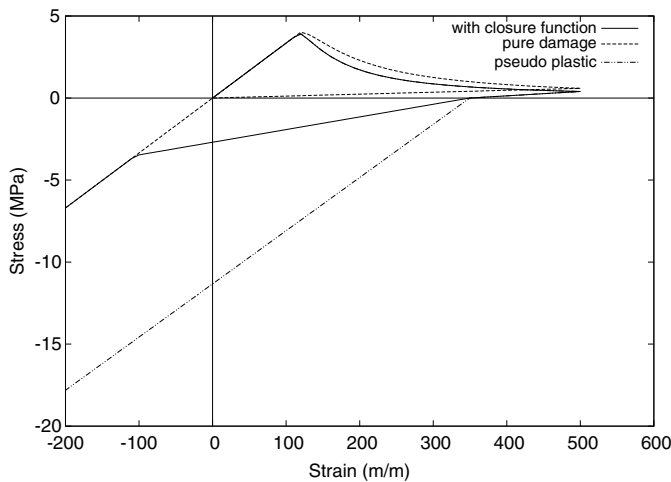

Fig. 2. Three point bending of a reinforced concrete beam: (a) computations for three sets of parameters; (b) experimental data

Fig. 3. Uniaxial behavior obtained for three sets of parameters

Cyclic Direct Tensile Test

In this paper, the authors attempted to characterize the opening and closure of macrocracks in a quasi-brittle specimen induced by cyclic compression/tension loadings. Specifically, the behavior of the concrete after tensile damage was studied.

Concrete loaded in tension brings to the fore the mechanism of crack propagation in the fracture process zone. During the uniaxial test, the stress tensor in the material is mainly uniaxial: Its value could be easily calculated, and the results are directly extendable to the model. Meanwhile, because of strain localization and the boundary-condition problems, the direct tension tests on quasi-brittle material are not easy to implement, thus explaining the few experiments conducted in this field.

First, the concrete heterogeneity, owing to the random distribution of aggregates of different sizes in the cement paste, causes a variation in the mechanical properties within the same sample. The macrocrack formation is then difficult to localize in such material. Furthermore, several cracks could be initiated and would propagate at the same time (Hordijk and Reinhardt 1990), creating hysteresis (Bazant and Planas 1997). Finally, cracks resulting from flexural stress could be generated because of eccentric loading. The experimental difficulty in performing a pure tensile test is associated with the nonsymmetrical distribution of local stresses in heterogeneous materials. Also, these problems yield unstable cracks very difficult to localize and, thus, to study.

To eliminate these concerns, studies have been carried out under different conditions to observe the influence of experimental parameters (Van Mier and Van Vliet 2002): the loading (Carpinteri and Ferro 1994; Carpinteri et al. 1994; Koide et al. 1997; Van Mier and Nooru-Mohamed 1990; Van Vliet and Van Mier 2000), the shape of the specimen, the presence of notches on the sample
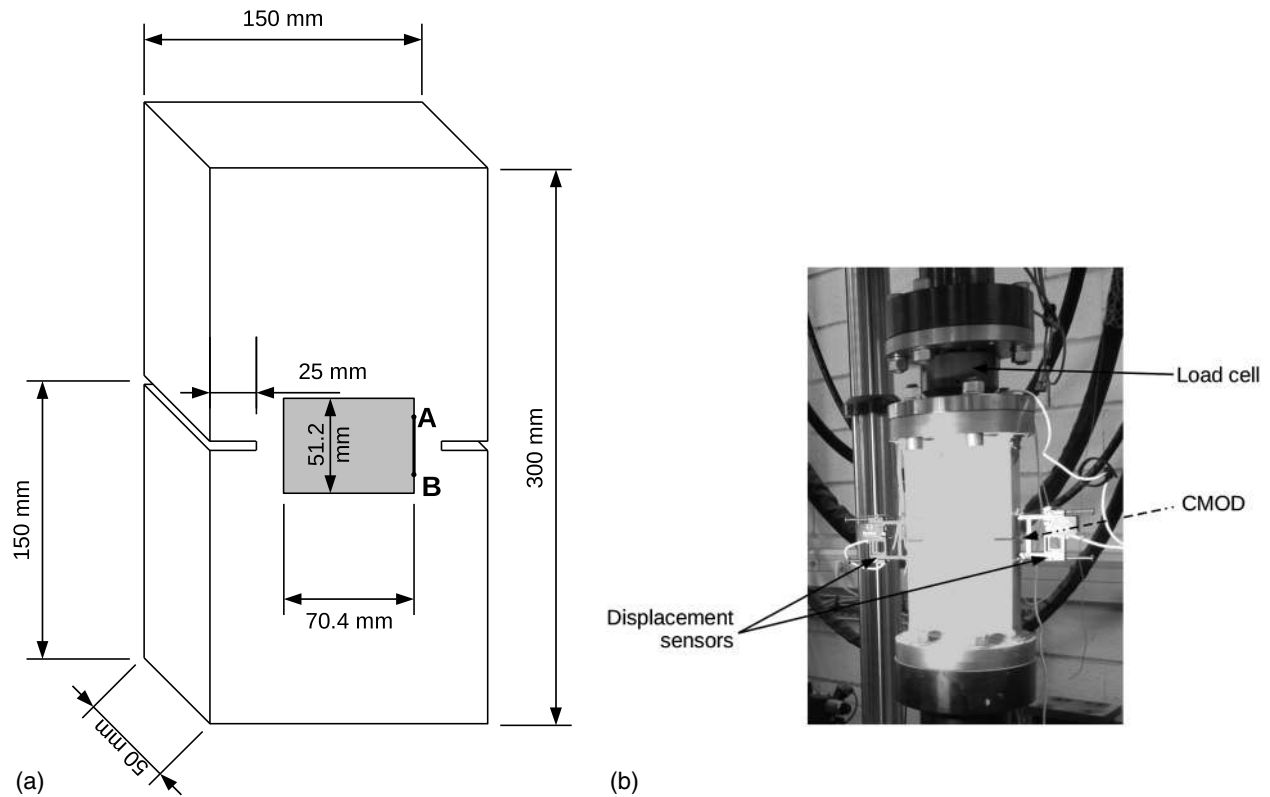
Fig. 4. (a) Specimen design and studied area for DIC (gray area); (b) setup

(Akita et al. 2003), and the hydric state of the material (Carpinteri and Ferro 1994; Koide et al. 1997; Ragueneau et al. 2000; Cornelissen et al. 1986). Some of these results tend to be contradictory. Therefore, a unique and consensual experimental protocol could not be set, and experimental parameters must be adapted in relation to the investigated phenomenon.

Materials

Shape

Notched prismatic specimens are chosen in order to control the position of the cracks; flat surfaces allow image analysis. The height of the specimen ensures test stability: The maximum strain reached at the end of the test must be greater than the peak strain. A simple analysis using linear fracture mechanics imposes a minimum height of 300 mm for a target value of a fracture energy of 101 $J \cdot m^{-2}$ (Nouailletas 2013). The width (50 mm) is chosen in relation to the maximum aggregate size. The specimen dimensions are 300 mm high, 150 mm length, and 50 mm width [Fig. 4(a)]. In order to accurately monitor the post-peak behavior of the sample, crack propagation must be stable during testing (Akita et al. 2003). Therefore, primary notches were created in the middle of the concrete specimen (Zhou 1995) to prevent macrocrack generation by concentrating overstresses around them. The studied area for digital image correlation (DIC) could then be restricted to the section surrounding these notches [Fig. 4(a)]. Two displacement sensors with 50 mm length were attached at both sides of the notches [Fig. 4(b)].

The notches were made 28 days after concrete casting and at least 24 h prior to testing by sawing under a water flow in order to limit damage to the material.

Concrete Mixture and Characteristics

The concrete mixture is detailed in Table 1. The specimens were cured in water (20°C) for at least 28 days prior to testing.

Table 2 summarizes the concrete's characteristics. The tests were performed on at least three samples; the mean value and the standard deviation are presented. The splitting tensile test and the compressive tests were performed on cylindrical specimens (160 × 320 mm).

Experimental Setup and Loading Mode

Setup

The test rig is mounted on a servohydraulic testing machine (HB250, Zwick/Roel, Metz, France). The servocontrol system and the high stiffness of the frame allow control of the test, even in the case of localization that causes a snapback. The applied force is measured by a 50-kN load cell (in addition to the 250-kN load cell available with the machine). Two displacement sensors are attached on the opposite notched sides of the specimen, on both sides of the notch. The gauge length of the displacement transducers is initially equal to 50 mm. Because these sensors are autonomous, they

Table 1. Concrete Mix Design

Constituents	Mixture proportions (kg · m^{-3})
Cement CEM V/A 42.5 N	320
Siliceous sand 0/4 mm	895
Limestone gravel 6/10 mm	874
Limestone addition	120
Efficient water (W_{eff})	200
Superplasticizer (% cement mass)	0.60
W_{eff}/C	0.62

Table 2. Characteristics of the Concrete

Properties	Mean value	Standard deviation	Standard references
Compressive strength ($\sigma_{c,max}$) (MPa)	61.4	2.2	NF EN 12390-3 Francaise de Normalisation (NF) 2012a
Splitting tensile strength ($\sigma_{t,max,split}$) (MPa)	4.9	0.5	NF EN 12390-6 Francaise de Normalisation (NF) 2012b
Young's modulus E(GPa)	37.9	5.8	NF EN 12390-3 Francaise de Normalisation (NF) 2012a
Porosity ε (%)	16.2	0.2	AFPC-AFREM recommendations
Apparent density ρ(kg $\cdot$ m^{-3})	2,225	10	

Note: AFPC = Association Française Pour la Construction; AFREM = Association Française de Recherche et d'Essais sur les Matériaux et les Constructions.

Table 3. Relative Uncertainties of the Different Sensors

Sensor	Range	Manufacturer	Relative uncertainty with respect to the range of the sensor (%)
Displacement sensors	±2.5 mm	Epsilon	±0.5
CMOD	5 mm	Sandner	±0.25
Force cell	50 kN	Interface	±0.25
Force cell	250 kN	Zwick/Roell	±0.25

Note: CMOD = crack mouth–opening displacement sensor.

Table 4. Sequential Control of Stages

Stage	Control	Set off	Rate	Observations
1	50 kN load cell	−40 kN	−1 kN/s	Determination of the initial Young's modulus (3 times)
2	—	+2.1 kN	+1 kN/s	—
3	Displacement sensors	Manual	+125 μm/s	n cycles, referred C1 to C n
4	—	−40 kN	−125 μm/s	—

provide information about the deformation of the two sides independently. The measured displacement is equal to the sum of the material deformation between the two measurement points and the crack opening from the notches. A finite-element computation shows that the displacement around the notch is nearly constant during the elastic stage and more so when the crack is developed. As a consequence, the measurement given by the sensor can be supposed to be the ratio of the crack-opening displacement and the gauge length. A crack mouth–opening displacement sensor is added for the system's feedback. All signals are recorded and synchronized through a multichannel digital controller. The uncertainties of the different sensors provided by the manufacturer (Grégoire et al. 2013) are summarized in Table 3.

A digital camera PixeLINK (Pixek Link, Ottawa, Ontario) equipped with a 70.4 telecentric lens allows the observation of crack initiation and propagation. The study area (70.4 × 51.2 mm, Fig. 4) corresponds to 3,000 × 2,182 pixels, and the use of a telecentric lens overcomes the spurious measurements due to out-of-plane displacements. During the test, pictures are acquired automatically at the rate of 10 frames per second. The lighting is controlled with an light-emitting diode (LED) bar. The images are then processed with an algorithm named CORRELI^{Q4} (Hild and Roux 2008). Initially developed for continuous problems, this algorithm has been improved for discontinuous problem (Mauroux et al. 2012). The size of the elements generated by CORRELI^{Q4} are equal to the pixel size. The uncertainty from the correlation is lower than 0.1 pixel, representing 2.35 μm in this study.

Solicitation Stages

The sequential control of stages applied during the test is summarized in Table 4. At the beginning of the test, three cycles of compression are performed to determine the initial Young's modulus of the material. The compressive load does not exceed 40 kN (less than 30% of the maximal compressive strength). Afterwards, positive displacement is imposed on the specimen (Stage 3) until the operator stops manually. A negative displacement is then applied up to a −40 kN load (Stage 4). The average value of the two displacement sensors monitors these displacements. The cycle (Stage 3 + Stage 4) is reached 10 times until the eleventh cycle, where the specimen is expected to break apart.

Three tests were performed during the experimental program, and results are detailed in Fig. 5. Fig. 5(a) shows the stress–strain

envelop curve for the three tests performed; it can be seen that, the tests are likely reproducible. The following analysis uses the results of Tests 2 and 3, because of the low number of cycles (n) in Test 1 ($n = 3$). In Figs. 5(b and c), the strain–stress curves of the tests later studied (Test 2: $n = 11$; Test 3: $n = 9$, the target number of 11 cycles was not reached because of the early failure of the sample). The normal stress, σ_n (MPa), is calculated from the value indicated by the 50-kN load cell divided by the cross-section area and is corrected by taking into account the saw cuts. The normal strain, ε (mm/mm), is the average value calculated from the displacements measured by the two sensors. In both cases, the shapes of the curves are similar to the results found in the literature (Reinhardt and Cornelissen 1984; Cornelissen et al. 1986): a variation of the stiffness during the cycle (Stages 3 and 4) can be observed, the stiffness degradation relative to the damage of the material, and the increase of the inelastic strain during the full test.

Eccentric Tension: Lateral Flexure

The concrete specimen is glued into the testing machine via steel plates (thickness: 25 mm) fixed with four bolts (diameter: 16 mm) in the piston's axis. To ensure the reproducibility of the tests, all the specimens are tested in the same initial conditions of saturation, i.e., 100% wet, ensured by immersion in water tanks until testing.

The primary difficulty of a direct tensile test is to maintain a constant and uniform load on the sample in order to avoid its rotation. This phenomenon could be caused by an eccentric loading, the heterogeneity of the material, or the anisotropy occurring after crack initiation (Cornelissen et al. 1986).

Fig. 6 shows the curves of the normal stress, σ_n (MPa), versus the vertical strain during the elastic cycle (first cycle C1), for each displacement sensor (ε_1 and ε_2) of Test 3. Because both curves are similar, it could be presumed that no rotation occurred during the elastic phase. The setup tends to minimize the phenomenon of lateral bending (or rotation) induced by the possible eccentricity of the load. Fig. 7 presents these full stress–strain curves for Test 3. The curves of ε_1 and ε_2 diverge after the peak load. This asymmetry is progressively marked during cycles. Although various experimental precautions have been taken, a slight rotation of the upper part of the specimen occurred. This could be attributed to the heterogeneity of the concrete, the initiation and propagation of the crack, or the flexibility induced by the load cell.
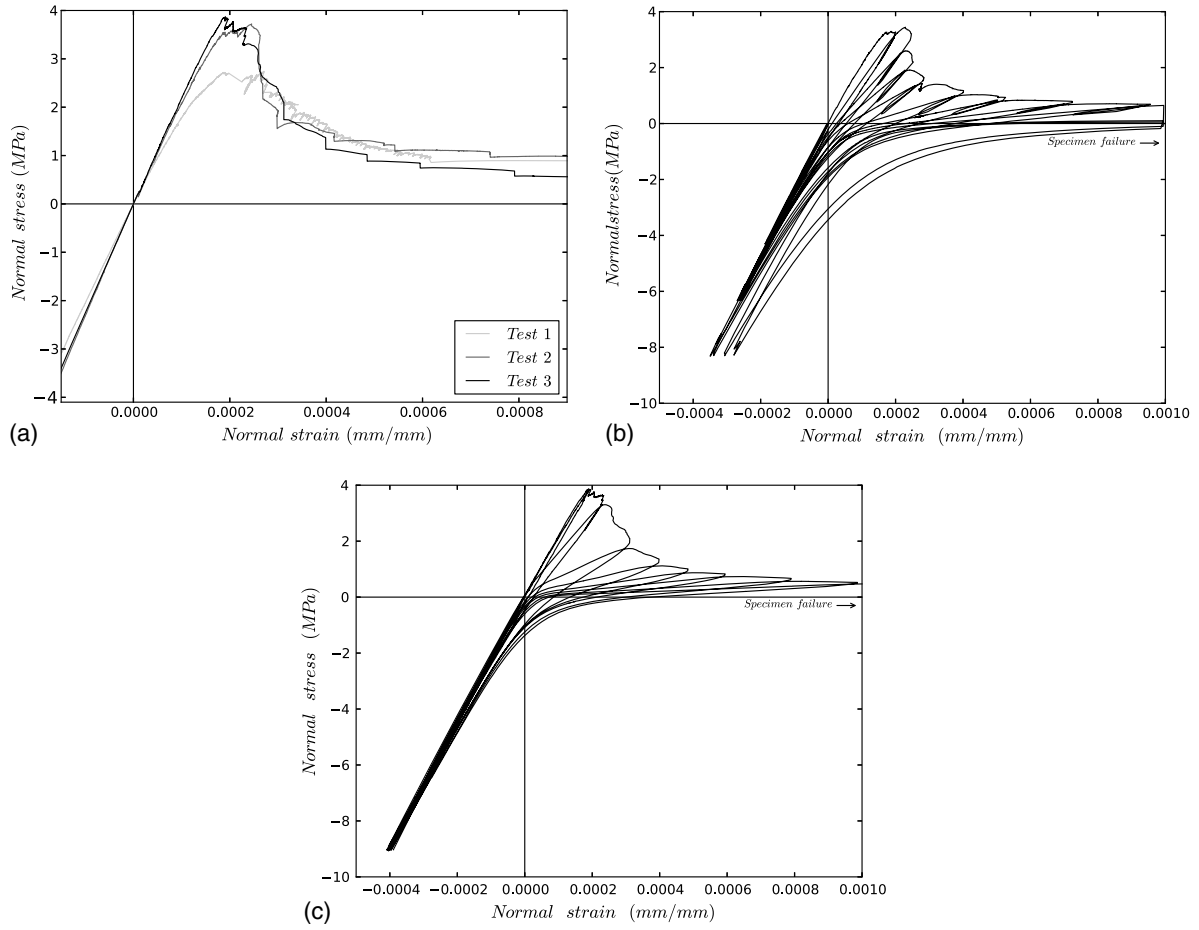
Fig. 5. Stress–strain curves of complete cyclic tension–compression test: (a) envelop curves of the three tests; (b) Test 2; (c) Test 3
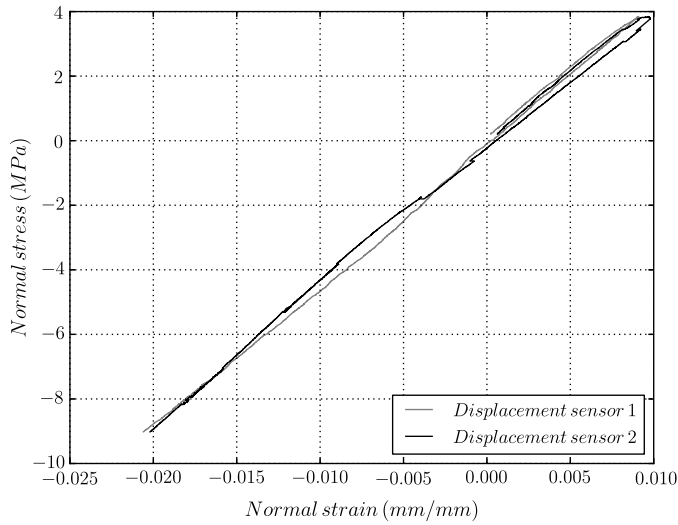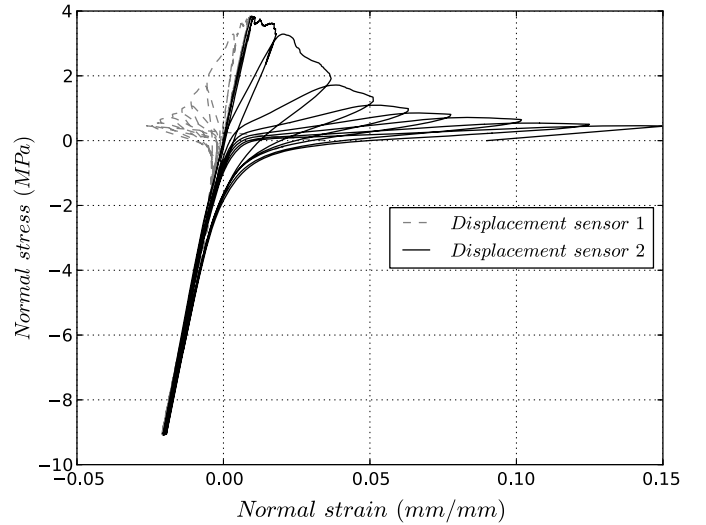

Fig. 6. Stress–strain curves for ε_1 and ε_2 during elastic cycle C1

Fig. 7. Stress–strain curves for ε_1 and ε_2 during the complete cyclic test (C1–C10)

To quantify this rotation, θ angle is determined from Eq. (1) (Fig. 8):

$$\theta = (h_1 - h_2)/2 \qquad (1)$$

Fig. 9 shows the evolution of θ angle during C6. The minimal rotation angle, $\theta_{\min}$, is calculated at the beginning of the compression

phase for the maximal stress. The maximal rotation angle, $\theta_{\max}$, is obtained at the maximal deformation of the cycle during tensile loading. During Stage 3, the rotation angle increases from $\theta_{\min}$ to $\theta_{\max}$. During Stage 4, the rotation angle decreases and tends toward zero, but it does not reach its initial value, $\theta_{\min}$, at the end of the cycle. Thus, $\theta_{\min}$ for C7 is greater than $\theta_{\min}$ for C6. Fig. 10
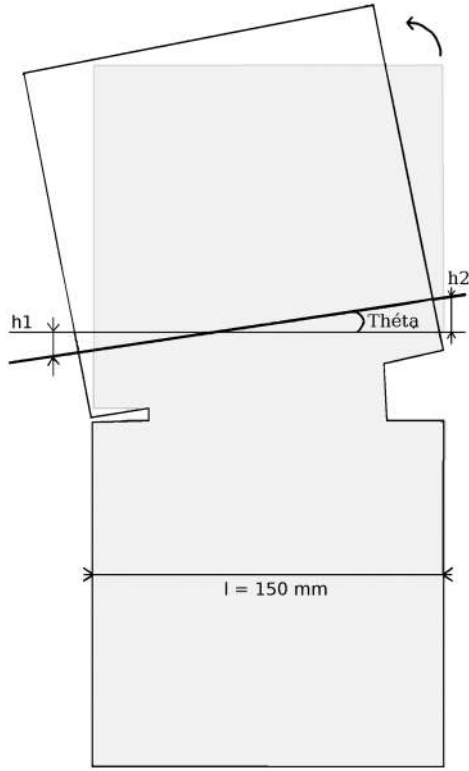
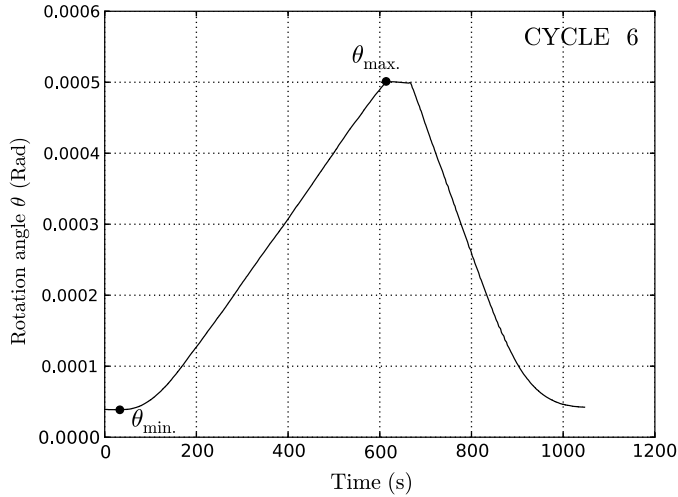**Fig. 8.** Illustration of the rotation θ

Fig. 9. θ angle during C6

illustrates the variation in the extreme values of the rotation angle ($\theta_{\min}$ and $\theta_{\max}$) during each cycle of the test (C1 to C10). The value $\theta_{\max}$ of each cycle increases with the damage of the material until C9. For the last cycle, C10, the $\theta_{\max}$ value decreases. The rotation phenomenon is diminished by the remarkable crack development that becomes predominant. The maximal value for $\theta_{\min}$ is reached at C7. After this cycle, the three last values decrease and become negative (for C9 and C10). The positive values of $\theta_{\min}$ show the residual rotation angles at the end of the compressive phases: $\theta_{\min}(C_{i+1}) > \theta_{\min}(C_i)$. The upper part of the sample does not return to its initial position because of the mismatching of the crack lips. The negative values of $\theta_{\min}$ at the end of the test could result in the lips' erosion induced by the cyclic loadings.
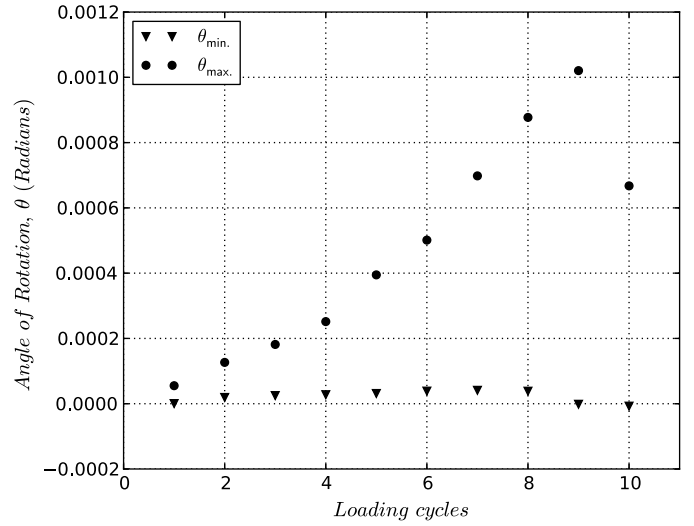

Fig. 10. Evolution of $\theta_{\min}$ and $\theta_{\max}$ during the cyclic test

The study of the lateral flexure during cyclic testing confirms the nonuniform strain distribution on the cross section as described by Cornelissen et al. (1986). This eccentricity is essentially governed by the dissymmetry induced by cracking, because of the heterogeneity of the concrete.

Results and Discussion

Tension–Compression Test Analysis

#### Cycles, Intercycles, and Envelope Curve

Fig. 11 shows the stress–strain curve of the complete cyclic tension–compression Test 1. A cycle is described by a tensile loading (Stage 3) and a compressive loading (Stage 4). This definition characterizes the damage of the material during the test. To make the diagram easy to read, only cycles C1, C4, C5, C6, and C11 are plotted. Here P_i represents the maximal tension stress of Cycle i.

The envelope curve of the test (Fig. 11) is derived from the superposition of the maximum stresses of each cycle and is similar to the curve of a monotonic tension test (Yankelevsky and Reinhardt 1989). So, the positive area under the envelop curve [Fig. 11(b)] multiplied by the average initial opening of the displacement sensors (l_0) gives the total fracture energy of the test, $G_f(\text{J} \cdot \text{m}^{-2})$

$$G_f = l_0 \int \sigma(\varepsilon) \cdot d\varepsilon = \int \sigma d\delta \tag{2}$$

with G_f = fracture energy (J $\cdot$ m^{-2}); $l_0 = 0.05$ m = average opening of extensometers at the beginning of the test (m); σ = tension stress (MPa); δ = crack opening (mm); and ε = normal strain (mm/mm).

The fracture energy, $G_{f,i}$, was calculated for each cycle i (Table 5). This parameter characterizes the propagation of cracks and the damage state of the material. During Test 3, the sample broke early during C9; in addition, $G_{f,9}$ is not the total fracture energy of this test, because the envelop curve did not reach zero stress. Then, the total fracture energy of Test 2, $G_{f,\text{tot}} = 100.93$ J $\cdot$ m^{-2}, is reached for Test 3.
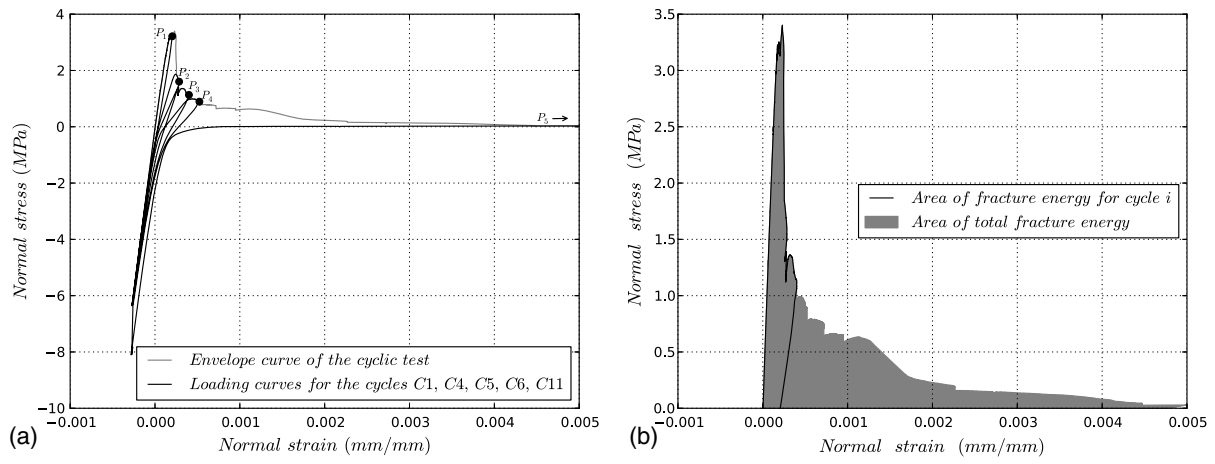
**Fig. 11.** (a) Envelop curve of a cyclic tension-compression test; (b) area used to fracture the energy calculus

Table 5. Fracture Energy Dissipated at Each Cycle

Cycle i	C1	C2	C3	C4	C5	C6	C7	C8	C9	C10	C11
					$G_{f,i}(\mathrm{J \cdot m^{-2}})$						
Test 1	6.75	12.56	18.56	24.01	32.60	38.53	45.82	52.18	82.52	96.21	100.93
Test 2	2.51	10.38	28.63	38.70	44.52	49.38	56.37	61.86	72.20	—	—

Image Correlation

The images of Fig. 12 represent the vertical displacement fields, obtained from the DIC algorithm CORRELI[Q4] (Hild and Roux 2008; Mauroux et al. 2012), at the maximal deformation for cycles C1, C4, C5, C6, and C11 during Test 1 [Fig. 11(a)]. The final crack pattern is superimposed to all images (black line) and the isovalues are adapted for each picture to easily observe the discontinuity of the vertical displacement field (macrocrack propagation).
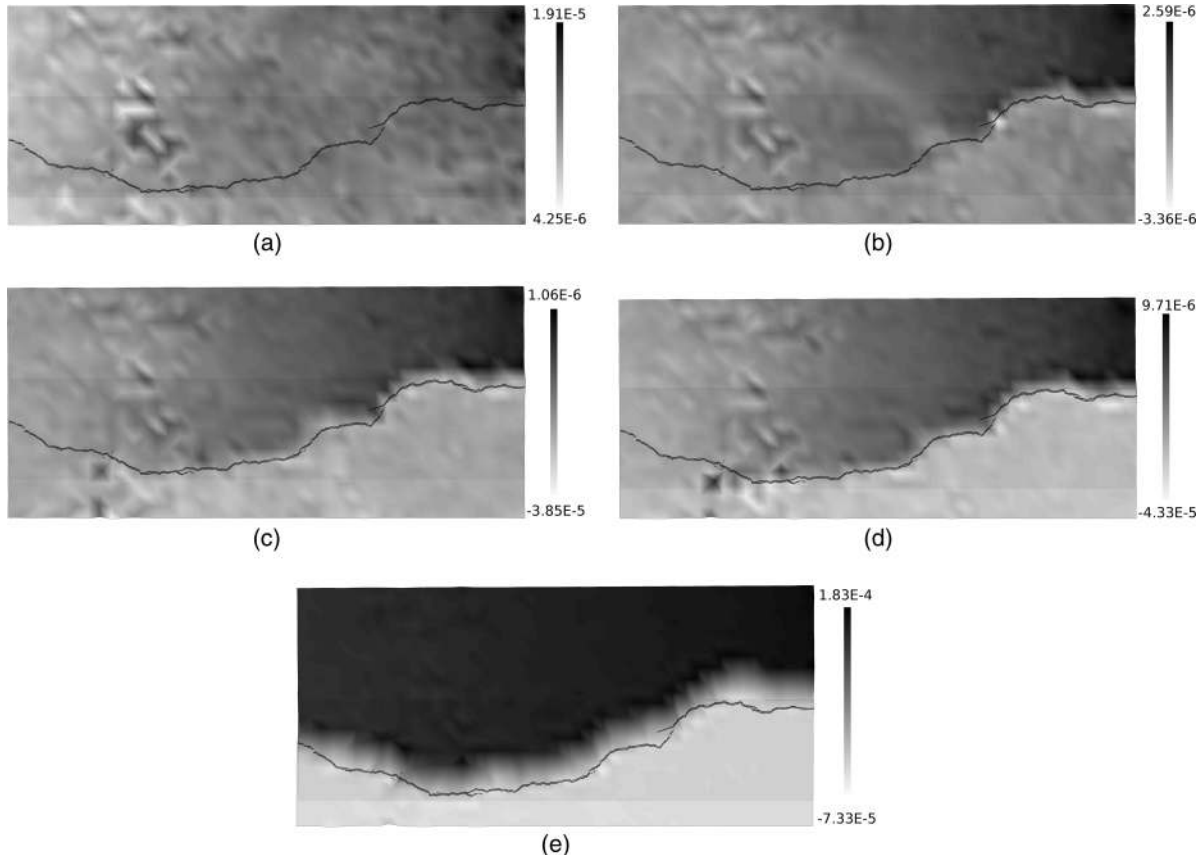
Fig. 12. Vertical displacement fields calculated by CORRELIQ4: (a) C1; (b) C4; (c) C5; (d) C6; (e) C11
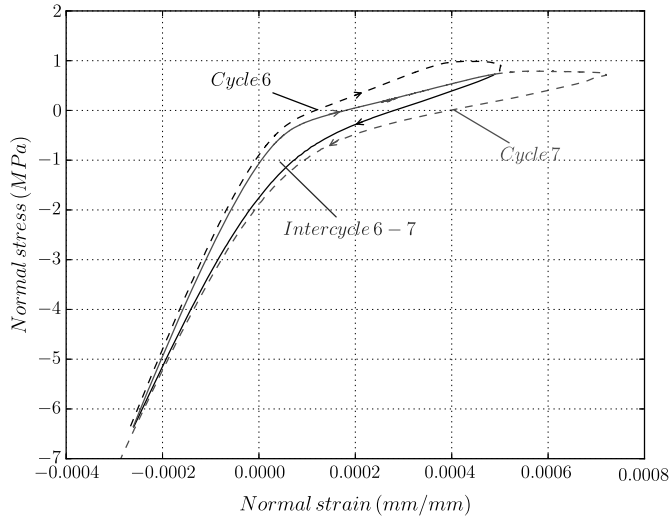
Fig. 13. Stress–strain curves of C6 and C7

Fig. 14. Calculation of damaged Young's modulus

The accuracy of the correlation analysis (2.35 μm) limits the study to the observation of macrocracks and their propagation in a qualitative way. The dark zones illustrate the maximal positive values of the vertical displacements at the moment of the picture capture (extension) and the bright zones illustrate the minimal values. The progression of the crack is clearly visible and confirms that, at the beginning of the cracking stage, the problem becomes asymmetric.

Cracking: Damage and Inelastic Strain Evolution

Damage (D) is defined as the degradation of the material's stiffness. To quantify this softening, the damage is calculated from the relative decrease of Young's modulus

$$D = 1 - (E_d/E) \tag{3}$$

with D = damage (–); E_d = damaged Young's modulus (GPa); and E = initial Young's modulus calculated with the three initial compressive loadings (GPa).

The damaged Young's modulus (E_d) is calculated during intercycles for positive stress.

An intercycle is defined by the union of two successive cycles, i and $i + 1$ (Fig. 13), and includes the tensile unloading of Cycle i, the compressive loading of Cycle i, the compressive unloading of Cycle $i + 1$, and the tensile loading of Cycle $i + 1$. The upper limit of the intercycle is the intersection between the tensile unloading of Cycle i and the tensile loading of $i + 1$. Beyond the normal strain corresponding to this intersection, the stiffness of the sample drops dramatically. Therefore, during an intercycle, the damage induced by the opening of new tensile microcracks is constant.

The value of the damaged Young's modulus is the slope derived from the linear regression of the mean values of tensile stress between the unloading curve i and loading curve $i + 1$. For example, in Fig. 14 (Intercycles 6 and 7), the damaged Young's modulus =2.90 GPa, and the damage $D = 0.92$.

Fig. 15 illustrates the evolution of damage, D, as a function of the relative fracture energy dissipated during a cycle for the two tests. Experimental data ($x = G_{i,f}/G_{f,\text{tot}}$, $y = D$) could be fit with an exponential function using a Levenberg–Marquardt algorithm:

$$D(G_{f,i}/G_{f,\text{tot}}) = 1 - \exp^{-G_{f,i}/(0.21 \times G_{f,\text{tot}})} \tag{4}$$

The theory of linear fracture mechanics suggests the amount of dissipated energy is proportional to the area of the created crack. On the other hand, the theory of damage proposed by Kachanov
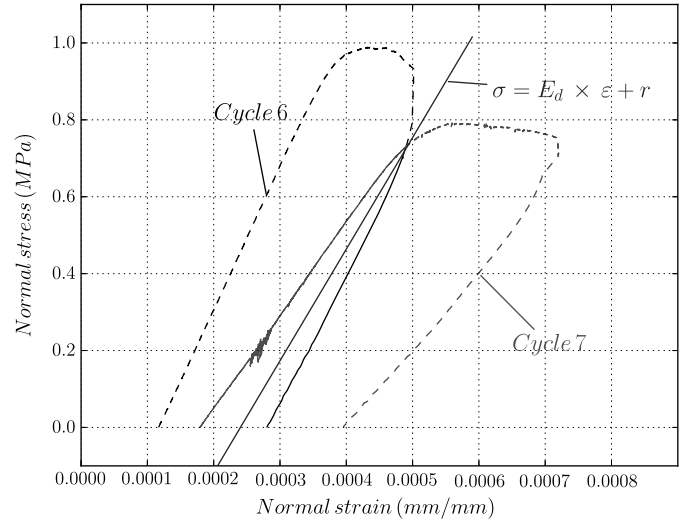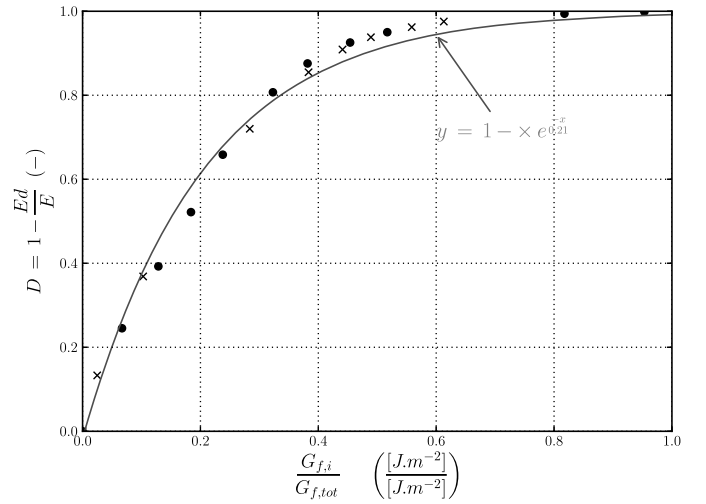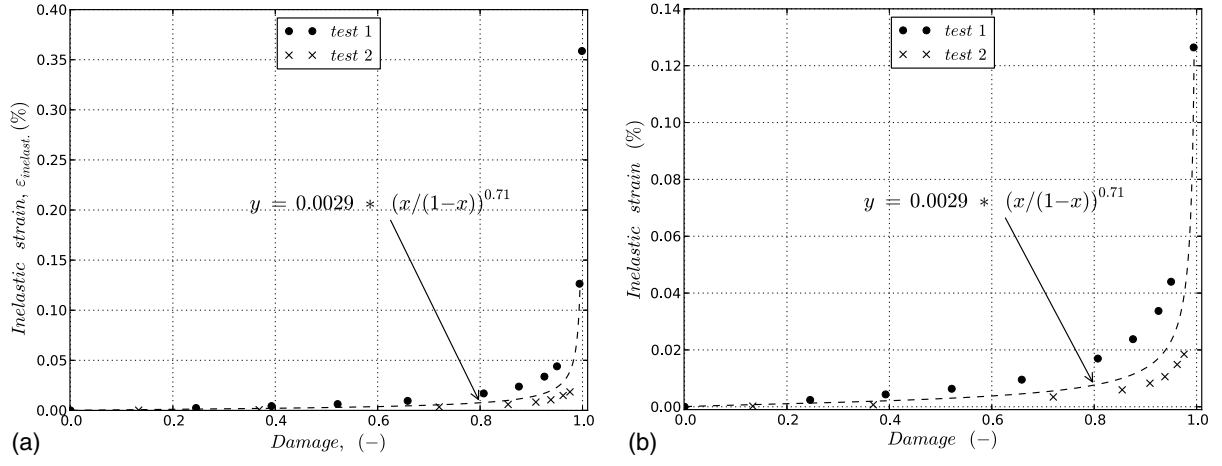

Fig. 15. Evolution of the damage as a function of dissipated fracture energy

(1958) and referred by Lemaitre (1996) supposes that the value of damage is the density of defects. This suggests that the relation between the damage and the dissipated energy is linear. Owing to the presence of a fracture-process zone, a part of the dissipated energy is the result of microcracking weakly affecting the stiffness. In addition, the damage is localized, and the Kachanov theory supposes the damage is distributed; however, that is not the case in this study. The nonlinearity of the relation between fracture energy exhibited in these experiments must be studied more deeply with numerical support to better understand the physical meanings.

The inelastic ε^{in} strain is defined as the residual deformation for zero stress. In Fig. 14, it is determined when the average curve tends toward zero.

The evolution of the inelastic strains as a function of the damage is presented in Fig. 16, showing the results of both tests. The link between damage and inelastic strains has been suggested by Hermann (Hermann and Kestin 1989) and La Borderie (La Borderie et al. 1994) who proposed the following relation, where β is a material parameter:

Fig. 16. Evolution of inelastic strains as a function of the damage: (a) all points; (b) zoom for inelastic strain less than 0.14%

$$\varepsilon^{\text{in}} = \beta[D/(1-D)] \tag{5}$$

On the basis of experimental data, a better fit can be found using the following equation:

$$\varepsilon^{\text{in}} = \beta[D/(1-D)]^{\alpha} \tag{6}$$

These results indicate the link between fracture energy, damage, and inelastic strains. These parameters could help to predict the crack propagation in quasi-brittle materials and improve current models.

Macrocrack Closure

Tangential Displacement
Macrocracks can be identified from Cycle 4 [Fig. 12(b)] through the discontinuity of the displacement field values. The closure behavior of the crack is studied from Cycle 6 of Test 1 (Fig. 17). The dotted black curve is drawn from experimental data and is the average of the loading/unloading stages, so as to disregard the hysteresis at this stage.

The black line represents the original elastic behavior, and the gray line represents the unloading linear behavior in C6.
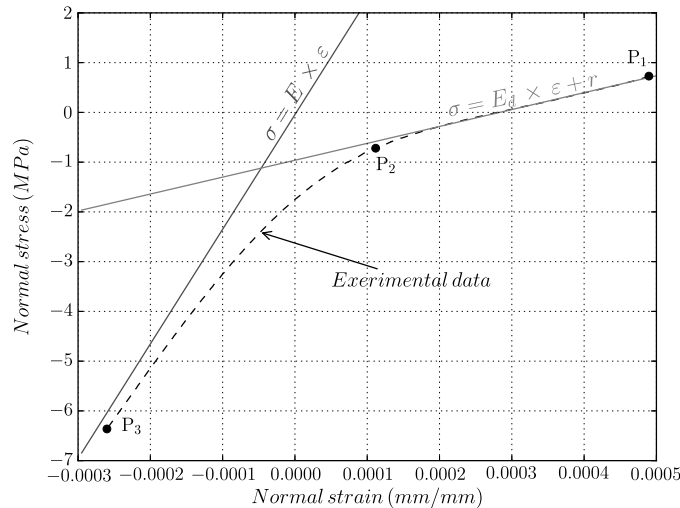
Fig. 17. Closure behavior during C6

The experimental behavior is asymptotic to these two lines and proves that the inelastic strains are vanishing when loading in compression mode. The fitting of these data could be approached by the equation:

$$\sigma = E(1-D) \cdot (\varepsilon - \varepsilon^{\text{in}}) \tag{7}$$

The closure behavior during C6 is analyzed with DIC at the three points indicated on the curve; pictures in Fig. 18 show the vertical displacement fields obtained with CORRELI^{Q4} at these moments: P_1, P_2, and P_3.
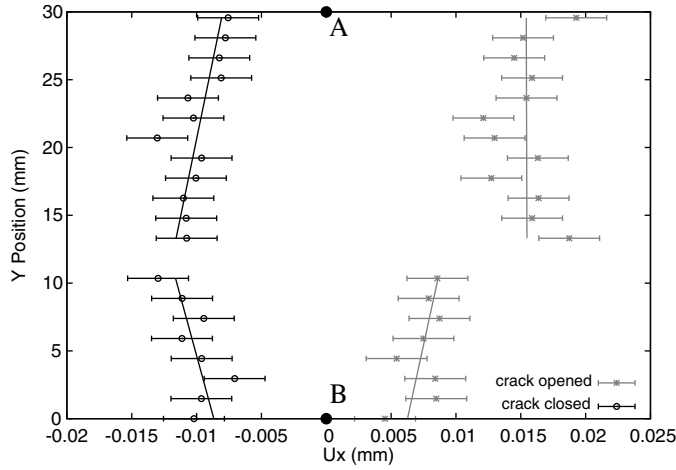
The value of P_1 corresponds to the maximum of the tensile stress for the studied cycle. At this point, the macrocrack is opened [Fig. 18(a)]. The nonlinear behavior initiates from point P_2. Because the stress state is negative, the crack should be closed. However, Fig. 18(b) shows remarkable differences between the vertical displacement values on both sides of the crack (right part of the picture); the discontinuity is opened. On the left part of the picture, the field is continuous, and the crack is considered as closed. Along the crack, the values of vertical displacements are not constant, inferring a heterogeneous stress field. They indicate localized contact zones between the lips of the crack where the material could be locally damaged. Because the contact is nonlinear, as expected, this forced re-engagement of the crack asperities causes nonlinear behavior (Gentier 1986). At the point P_3, the values of the vertical displacement field are likely homogeneous on the DIC area; the crack is now closed. For higher compressive stress states, the sample remains in the elastic phase because the total contact between the two lips ensures a continuous transmission of the stresses.

The study of the closure during C6 was completed with an analysis of horizontal displacements (Fig. 19) on the segment [AB] shown in Fig. 4. Horizontal displacements for the opened and closed crack are represented in gray and black, respectively. These points correspond to the position of the mesh nodes generated by CORRELI^{Q4}. Error bars represent the uncertainty generated by the correlation calculation. For linear and continuous deformations, the horizontal displacements remain on the [AB] segment, and a straight line can be plotted between all the nodes.

When the crack is closed at Cycle 6, a straight line between points A and B can be drawn considering the nonaberrant intervals. The horizontal displacement of the profile can be assumed to be continuous. However, during opening, there is a shift of 5 μm consequent to the crack slip. The crack slip displacements may be the cause of the inelastic strain and of the hysteresis (Jefferson 2003; Sellier et al. 2013).
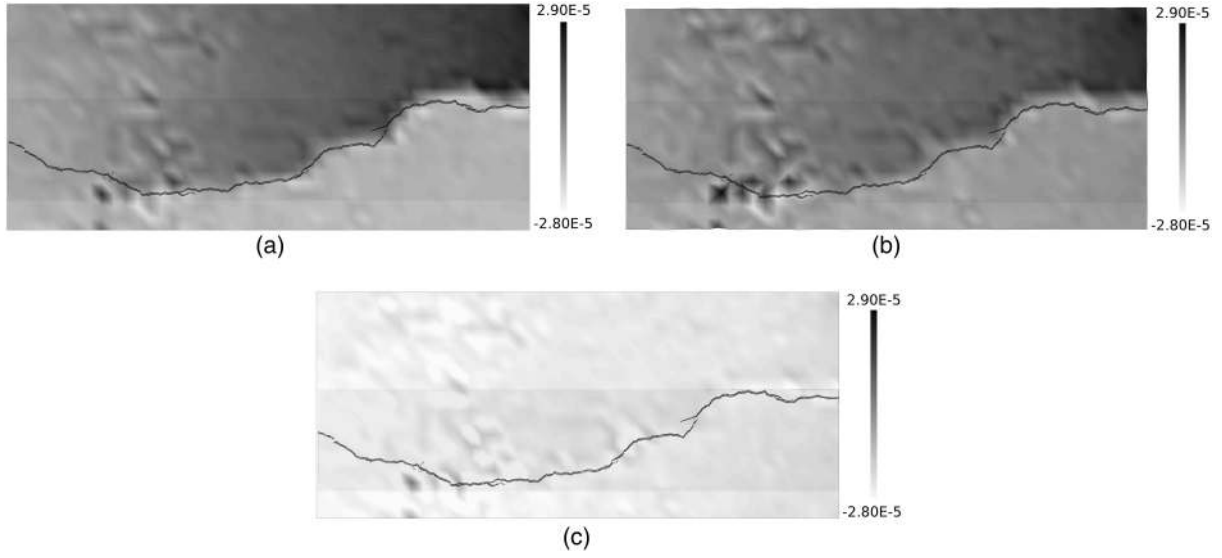
Fig. 18. Vertical displacement fields calculated by CORRELI^{Q4} at P1, P2, and P3: (a) opened crack; (b) contact between the lips of the crack; (c) closed crack

Fig. 19. Horizontal displacements

Fig. 20. Evolution of the relative dissipated friction energy as a function of damage
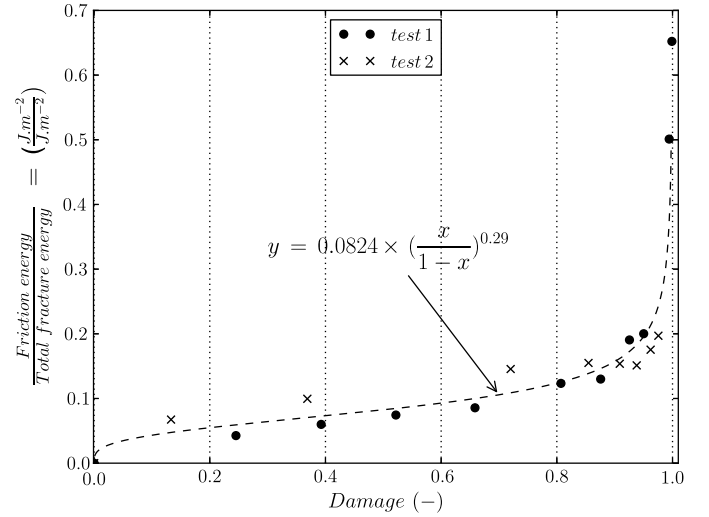
Energy Dissipated by Friction

The friction between two surfaces dissipates energy. For a cyclic tension–compression test, this phenomenon causes a hysteresis between two cycles observed on the stress–strain curve. To characterize the evolution of this energy during crack propagation, the analysis focuses on the intercycles defined above, where the damage level of the material is constant.

The energy dissipated by friction, w_f, was evaluated by calculating the area of an intercycle (Fig. 13)

$$w_f = l_0 \int_{\text{intercycle}} \sigma \cdot (\varepsilon) d\varepsilon \qquad (8)$$

The energy dissipated by friction was computed for each intercycle. Fig. 20 shows the evolution of the relative friction energy (the ratio between the energy dissipated by friction on the total fracture energy) as a function of the damage parameter for both tests. A hyperbolic relationship provides good support for experimental data. For a state of damage near the failure, the energy dissipated by friction during the reclosing represents more than 30% of the total fracture energy.

This section underlines the nonlinear behavior of a macrocrack under cyclic normal loadings. The phenomenon of friction during the re-engagement phase is illustrated by the hysteresis formed between the two cycles. The DIC analysis shows the crack-slip displacements induced by the mismatching of crack lips. These phenomena could explain the presence of inelastic strain and hysteresis. However, the cracks are fresh and should normally match. This geometric difference could be explained by the existence of internal stresses in the material (Briffaut et al. 2013). Propagation of cracking induces a relaxation of internal stresses, which generates nonuniform strain on each side of the crack, creating nonadditional asperities.

Conclusion

This study allowed a better understanding of the quasi-brittle material behavior under cyclic loading and particularly during the phase of crack closure:

- The nonlinear behavior of the material in tension could be explained by damage and inelastic strains. The inelastic strains seem to be linked to damage, as the hyperbolic relationship fits the experimental data. Thus, these two variables should be thermodynamically dependent.
- During the compression phases, the inelastic strains progressively vanish and the material recovers its initial stiffness. The evolution of the inelastic strains during a crack closure can be partially explained by friction phenomena generated by the mismatching discontinuity lips. The energy dissipated by friction becomes significant for high values of damage and can reach the order of magnitude of the fracture energy. Furthermore, the evolution of the energy dissipation of cracking, damage, and inelastic deformations are linked.

Further investigations are still necessary to confirm these conclusions and to describe the relationships between damage, inelastic strains, and friction energy.

These experimental results obtained on concrete agree with those obtained by Reinhardt 30 years ago on mortar and will help the community that develops models used for cyclic loadings of concrete elements.

Acknowledgments

References

Akita, H., Koide, H., Tomon, M., and Sohn, D. (2003). "A practical method for uniaxial tension test of concrete." *Mater. Struct.*, 36(6), 365–371.

Bazant, Z. P., and Planas, J. (1997). *Fracture and size effect in concrete and other quasi-brittle materials*, CRC Press, Boca Raton, FL.

Berthaud, Y., La Borderie, C., and Ramtani, S. (1990). "Damage modelling and crack closure effect." *Damage Mech. Eng. Mater.*, 109(1), 263–276.

Briffaut, M., Benboudjema, F., La Borderie, C., and Torrenti, J. M. (2013). "Creep consideration effect on meso-scale modelling of concrete hydration process and consequences on the mechanical behaviour." *J. Eng. Mech.*, 10.1061/(ASCE)EM.1943-7889.0000607, 1808–1817.

Carol, I., and Willam, K. (1996). "Spurious energy dissipation/generation in stiffness recovery models for elastic degradation and damage." *Int. J. Solids Struct.*, 33(20–22), 2939–2957.

Carpinteri, A., Ferrara, G., and Imperato, L. (1994). "Scaling laws for strength and toughness of disordered materials: A unified theory based on fractal geometry." *Eng. Fract. Mech.*, 48(5), 673–689.

Carpinteri, A., and Ferro, G. (1994). "Size effects on tensile fracture properties: A unified explanation based on disorder and fractality of concrete microstructure." *Mater. Struct.*, 27(10), 563–571.

Cornelissen, H. A. W., Hordijk, D. A., and Reinhardt, H. W. (1986). "Experimental determination of crack softening characteristics of normal weight and lightweight concrete." *Heron*, 31(2), 1–12.

NF (Francaise de Normalisation). (2012a). "Testing hardened concrete. Part 3 : Compressive strength of test specimens." *NF EN 12390-3* (in French).

NF (Francaise de Normalisation). (2012b). "Testing hardened concrete. Part 6: Tensile splitting strength of test specimens." *NF EN 12390-6* (in French).

Gentier, S. (1986). "Morphologie et comportement hydromécanique d'une fracture naturelle dans le granite sous contrainte normale–Étude expérimentale et théorique." Ph.D. thesis, Univ. of Orléans, France (in French).

Grégoire, D., Rojas-Solano, L., and Pijaudier-Cabot, G. (2013). "Failure and size effect for notched and unnotched concrete beams." *Int. J. Numer. Anal. Methods Geomech.*, 37(10), 1434–1452.

Hermann, G., and Kestin, J. (1989). "Strain localization and size effects due to damage and cracking." *On thermodynamic foundation of a damage theory in inelastic solids*, J. Mazars and Z. P. Bazant, eds., Elsevier, London, 228–232.

Hild, F., and Roux, S. (2008). "CORRELIQ4 : A software for" finite-element" displacement field measurements by digital image correlation." *Interne Rep. 269*, Hild and Roux, LMT-Cachan, Cachan, France.

Hordijk, D. A., and Reinhardt, H. W. (1990). "Fracture of concrete in uniaxial tensile experiments as influenced by curing conditions." *Eng. Fract. Mech.*, 35(4–5), 819–826.

Jefferson, A. D. (2003). "A plastic-damage-contact model for concrete. I. Model theory and thermodynamic considerations." *Int. J. Solids Struct.*, 40(22), 5973–5999.

Kachanov, L. M. (1958). "On creep rupture time." *IVZ Akad. Nauk. S.S.R. Otd. Tech. Nauk.*, 97(1–4), 26–31.

Koide, K., Akita, H., and Tomon, I. H. (1997). "A direct tension test for obtaining tension softening curves of unnotched concrete specimens." *Brittle Matrix Composites 5*, A. M. Brandt, V. C. Li and I. H. Marshall, eds., BIGRAF and Woodhead, Warsaw, 336–375.

La Borderie, C., Mazars, J., and Pijaudier-Cabot, G. (1994). "Response of plain and reinforced concrete structures under cyclic loadings." *Am. Concr. Inst.*, 134, 147–172.

Lemaitre, J. (1996). *A course on damage mechanics*, Springer, Berlin.

Mauroux, T., Benboudjema, F., Turcrya, P., Aït-Mokhtara, A., and Deves, O. (2012). "Study of cracking due to drying in coating mortars by digital image correlation." *Cem. Concr. Res.*, 42(7), 1014–1023.

Mazars, J., and Berthaud, Y. (1989). "Une technique expérimentale appliquée au béton pour créer un endommagement diffus et mettre en évidence son caractère unilatéral." *Comp. Rend. Acad. Sci. Ser. 2 Mecanique Phys. Chim. Sci. Univ. Sci. Terre*, 308, 579–584 (in French).

Mazars, J., Berthaud, Y., and Ramtani, S. (1990). "The unilateral behaviour of damaged concrete." *Eng. Fract. Mech.*, 35(4–5), 629–635.

Nouailletas, O. (2013). "Comportement d'une discontinuité dans un géomatériau sous sollicitations chemo-mécanique: Expérimentations et modélisations." Ph.D. thesis, Univ. of Pau, Pau, France.

Ragueneau, F., La Borderie, C., and Mazars, J. (2000). "Damage model for concrete-like materials coupling cracking and friction, contribution towards structural damping: First uniaxial applications." *Mech. Cohesive-Frict. Mater.*, 5(8), 607–625.

Reinhardt, H. W., and Cornelissen, H. A. W. (1984). "Post-peak cyclic behaviour of concrete in uniaxial tensile and alternating tensile and compressive loading." *Cem. Concr. Res.*, 14(2), 263–270.

Reinhardt, H. W., Cornelissen, H. A. W., and Hordijk, D. A. (1986). "Tensile tests and failure analysis of concrete." *J. Struct. Eng.*, 10.1061/(ASCE)0733-9445(1986)112:11(2462), 2462–2477.

Sellier, A., Casaux-Ginestet, G., Buffo-Lacarrière, L., and Bourbon, X. (2013). "Orthotropic damage coupled with localized crack reclosure processing. Part I: Constitutive laws." *Eng. Fract. Mech.*, 97, 148–167.

Van Mier, J. G. M., and Nooru-Mohamed, M. B. (1990). "Geometrical and structural aspects of concrete fracture." *Eng. Fract. Mech.*, 35(4–5), 617–628.

Van Mier, J. G. M., and Van Vliet, M. R. A. (2002). "Uniaxial tension test for the determination of fracture parameters of concrete: State of the art." *Eng. Fract. Mech.*, 69(2), 235–247.

Van Vliet, M. R. A., and Van Mier, J. G. M. (2000). "Experimental investigation of size effect in concrete and sandstone under uniaxial tension." *Eng. Fract. Mech.*, 65(2–3), 165–188.

Wu, J. Y., and Xu, S. L. (2013). "Reconsideration on the elastic damage/degradation theory for the modeling of microcrack closure-reopening (MCR) effects." *Int. J. Solids Struct.*, 50(5), 795–805.

Yankelevsky, D. Z., and Reinhardt, H. W. (1989). "Uniaxial behavior of concrete in cyclic tension." *J. Struct. Eng.*, 10.1061/(ASCE)0733-9445(1989)115:1(166), 166–182.

Zhou, Z. P. (1995). "Influence of notch size, eccentricity and rotational stiffness on fracture properties determined in tensile tests." *Fracture Mechanics of Concrete Structures, Proc.*, FRAMCOS-2, Folker H. Wittmann, Freiburg, 65–74.